Large fieldlike torque in amorphous Ru₂Sn₃ originated from the intrinsic spin Hall effect

Thomas J. Peterson [1,*] Mahendra DC [1,*] Yihong Fan,[2] Junyang Chen,[2] Delin Zhang,[2] Hongshi Li,[2] Przemyslaw Swatek,[2] Javier Garcia-Barriocanal,[3] and Jian-Ping Wang [1,2,†]

[1]*School of Physics and Astronomy, University of Minnesota, Minneapolis, Minnesota 55455, USA*
[2]*Electrical and Computer Engineering Department, University of Minnesota, Minneapolis, Minnesota 55455, USA*
[3]*Characterization Facility, University of Minnesota, Minneapolis, Minnesota 55455, USA*

We investigated temperature dependent current driven spin-orbit torques in magnetron sputtered Ru₂Sn₃ (4 and 10 nm)/$Co_{20}Fe_{60}B_{20}$ (5 nm) layered structures with in-plane magnetic anisotropy. The room temperature dampinglike and fieldlike spin torque efficiencies of the amorphous Ru₂Sn₃ films were measured to be $0.14 \pm 0.008 (0.07 \pm 0.012)$ and $-0.03 \pm 0.006 (-0.20 \pm 0.009)$, for the four (10 nm) films, respectively, by utilizing the second-harmonic Hall technique. The large fieldlike torque in the relatively thicker Ru₂Sn₃ (10 nm) thin film is unique compared to the traditional spin Hall materials interfaced with thick magnetic layers with in-plane magnetic anisotropy which typically have dominant dampinglike and negligible fieldlike torques. Additionally, the observed room temperature fieldlike torque efficiency in Ru₂Sn₃ (10 nm)/CoFeB (5 nm) is up to three times larger than the dampinglike torque (-0.20 ± 0.009 and 0.07 ± 0.012, respectively) and 30 times larger at 50 K (-0.29 ± 0.014 and 0.009 ± 0.017, respectively). The temperature dependence of the fieldlike torques shows dominant contributions from the intrinsic spin Hall effect while the dampinglike torques show dominate contributions from the extrinsic spin Hall effects, skew scattering, and side jump. Through macrospin calculations, we found that including fieldlike torques on the order of or larger than the dampinglike torque can reduce the switching critical current and decrease magnetization procession for a perpendicular ferromagnetic layer.

I. INTRODUCTION

Devices designed with spin-orbit torque (SOT) materials have been considerably studied as candidates for developing ultrafast-speed and ultralow-energy spin memory and logic applications, such as SOT magnetic random access memory (SOT MRAM) [1–3]. The most commonly studied SOT generators are heavy metals (HMs), such as Ta [1,4,5], W [6–8], Pt [9–11], and topological insulators (TIs), such as Bi₂Se₃ [12–18], $(Bi_xSb_y)_2Te_3$ [19,20], and Bi₂Te₃ [19]. HMs with low resistivities (10–300 $\mu\Omega$ cm [1,4–10,11]) have charge to spin and spin to charge conversion efficiencies (ζ_S) generated primarily by the bulk spin Hall effect, and have spin torque efficiency in the range of 0.01–0.5 [1,4–10,11]. However, TI materials with larger resistivities (1000–100 000 $\mu\Omega$ cm [12–19,20]) can have ζ_S much larger than 1. The efficient spin torque generation in TIs is due to spin polarized surface states where the electron's spin is perpendicularly locked with its momentum [12,14,21–23]. In addition to the spin-momentum locking, the bulk spin Hall effect [1,24] and the interfacial Rashba effect [9,25,26] can also generate spin torques in TI materials. The spin density generation in TIs has been shown to improve in nanocrystalline systems; sputtered Bi₂Se₃ has shown larger spin torque efficiencies (10–1000×) compared to single crystal molecular beam epitaxy grown Bi₂Se₃ due

to quantum confinement from the grain size reduction in dimensionality [15,17]. Recent calculations on amorphous TI materials have shown that spin polarized edge states can exist and maintain topological protection even in fully amorphous systems [27]. Spin polarized surface states have been observed via angle resolved photoemission spectroscopy (ARPES) in amorphous Bi₂Se₃ [28], and greater than 1 SOT efficiencies have been measured in amorphous Gd alloyed Bi₂Se₃ [29].

However, for SOT MRAM applications the typical metallic free layers can have large current shunting due to the high resistivity of TI SOT channels, increasing the critical current required for magnetization switching. Novel lower-resistivity topological materials are required to reduce the critical switching current density [30]. A possible new material is the Ru₂Sn₃ system. Ru₂Sn₃ is a low-resistivity TI material, with a resistivity ranging from 800 to 2000 $\mu\Omega$ cm (10× lower than sputtered Bi₂Se₃). The Ru₂Sn₃ band structure is a semiconductor at room temperature. Due to a crystalline phase change that occurs at 160 K, the band structure of the low-temperature phase becomes a TI with highly anisotropic surface states [31]. The TI surface states in the low-temperature phase have been observed through ARPES experiments [31]. The phase change is accompanied by a characteristic peak in resistivity centered at 160 K [32,33]. The low-temperature crystal phase has been experimentally shown to stabilize at room temperature via extreme applied pressures [34]. The Ru₂Sn₃ crystalline structure is also robust against annealing and stable up to 1100 °C, making it a

---

*These authors contributed equally to this paper.
†jpwang@umn.edu

possible candidate for industrial application and complementary metal oxide semiconductor (CMOS) integration [35].

In this paper, we report large fieldlike torques with non-negligible dampinglike torques in sputtered, amorphous Ru_2Sn_3 thin films. We confirm the amorphous structure of the films with high-resolution tunneling electron microscopy and the 2:3 composition with Rutherford backscattering techniques. Through the second-harmonic Hall measurement we can extract and characterize the effective dampinglike (DL) and fieldlike (FL) SOTs originating in the Ru_2Sn_3 films. We find room temperature ζ_S^{DL} of 0.14 ± 0.008 and 0.07 ± 0.012 and a ζ_S^{FL} of -0.03 ± 0.006 and -0.20 ± 0.009 for 4 and 10 nm Ru_2Sn_3 films, respectively. By analyzing the resistivity dependence of the spin torque efficiencies, we extracted the contributions from the intrinsic and extrinsic spin Hall effects. The FL torques show dominant contributions from the intrinsic spin Hall effect with intrinsic spin conductivity while the DL torques show dominate contributions from the extrinsic spin Hall effects, skew scattering, and side jump. We performed macrospin calculations of the Landau-Lifshitz-Gilbert (LLG) equation to simulate switching a magnetic layer including both the DL and FL torques generated from the Ru_2Sn_3 SOT channel. We find the inclusion of FL torques three times greater than the DL can reduce the critical current required for switching by almost 50% and reduce the magnetization precession compared to the DL torque only case.

II. MATERIALS GROWTH AND CHARACTERIZATION

To investigate the SOTs in Ru_2Sn_3, thin films of Ru_2Sn_3(4 nm, 10 nm)/$Co_{20}Fe_{60}B_{20}$(5 nm)/MgO(2 nm)/Ta(2 nm) were deposited using magnetron sputtering on 300 nm thermally oxidized Si wafers, with a base pressure of 9×10^{-8} Torr and an Ar working pressure of 1.5 mTorr. The 4 and 10 nm Ru_2Sn_3 samples are labeled as RS4 and RS10, respectively. The Ru_2Sn_3 thin films were sputtered from a pure Ru_2Sn_3 alloy target but due to the nonempirical nature of magnetron sputtering, the composition may slightly drift from the optimal value. To confirm the ratio of Ru to Sn, the composition has been measured using Rutherford backscattering (RBS), with a He^+ beam with maximum energy of 4.7 MeV and current of 40 μC, on a bare 17 nm Ru_2Sn_3 thin film, as shown in Supplemental Fig. 8(a) (Supplemental Material [36]). The final elemental composition is calculated from fitting the simulation results done in QUARK to the measured RBS data. The final composition of the sputtered Ru_2Sn_3 is calculated to be 40.2% and 59.8% (±0.15%), respectively. Additionally, tunneling electron microscope (TEM) measurements were done on the RS4 and RS10 samples and show an amorphous phase of the Ru_2Sn_3. The bright-field TEM and high-angle annular dark-field (HAADF) images of RS10 shown in Figs. 1(a) and 1(b) suggest that no crystalline structure is observed in the Ru_2Sn_3 layer with small crystallites in the $Co_{20}Fe_{60}B_{20}$ and MgO layers. Further investigation including selected area diffraction did not reveal any long-range order in the Ru_2Sn_3 layer, indicating this layer is amorphous throughout, as shown in Fig. 1(c). Further measurements of x-ray diffraction (XRD) and Raman spectroscopy on 17 nm Ru_2Sn_3 thin films showed no indication of crystal structure; however, both measurements are limited by the film thickness.
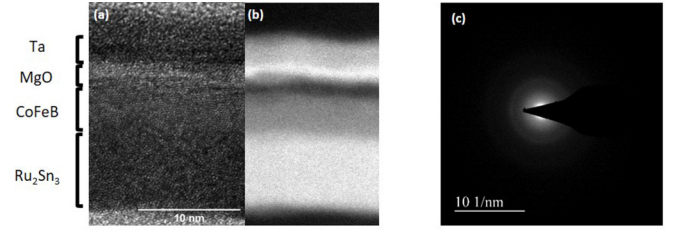

FIG. 1. (a) Bright-field transmission and (b) high-angle annular dark-field electron microscope image of the RS10 sample. (c) Selected area diffraction pattern of the RS10 sample. The diffuse ring seen suggests an amorphous film with no long-range order.

III. SECOND-HARMONIC HALL MEASUREMENT FOR SOT CHARACTERIZATION

To calculate the charge to spin conversion efficiency of the DL and FL torque contributions independently we utilize the harmonic Hall measurement technique [37–40]. The RS4 and RS10 samples were patterned into Hall bars with a length of 85 μm and a width of 10 μm. An AC current with frequency 133 Hz and peak value of 4 mA is applied through the channel. Figure 2(a) shows a schematic of the second-harmonic measurement. The Hall bar is rotated in the xy plane from $0°$ to $360°$, while the first- and second-harmonic Hall voltages are measured via two lock-in amplifiers. Figure 2(b) shows the resulting first-harmonic Hall voltage which provides the planar Hall resistance and can be fitted by

$$V_{xy}^{\omega} = R_{PHE} \sin 2\varphi \, I, \tag{1}$$

where φ is the in-plane angle. R_{PHE} is the planar Hall resistance. Figure 2(c) shows the second-harmonic Hall voltages and is given by

$$V_{xy}^{2\omega} = [V_{DL}\cos\varphi - V_{FL}(\cos2\varphi \, \cos\varphi)]I,$$
$$V_{DL} = \frac{1}{2}R_{AHE}\frac{-H_{DL}}{H_{ext} + H_k} + I\,\alpha\,\nabla T, \tag{2}$$
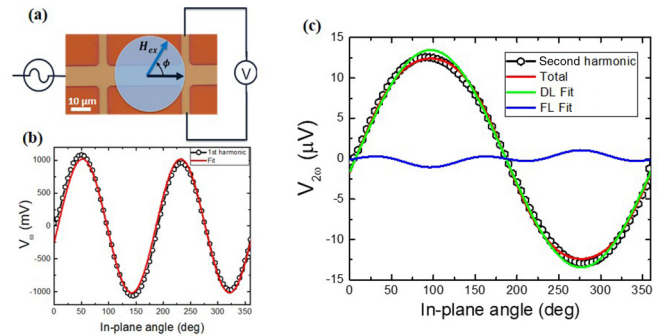$$V_{FL} = R_{PHE}\frac{H_{FL} + H_{Oe}}{H_{ext}},$$

FIG. 2. (a) Diagram of the harmonic Hall measurement: a Hall bar with a length of 85 μm and a width of 10 μm is rotated in the xy plane from $0°$ to $360°$, while the first- and second-harmonic Hall voltages are measured via two lock-in amplifiers. (b) The first-harmonic and (c) second-harmonic Hall voltages for the RS10 sample rotated in a 1500 Oe external field at 300 K fitted to Eqs. (1) and (2), respectively.
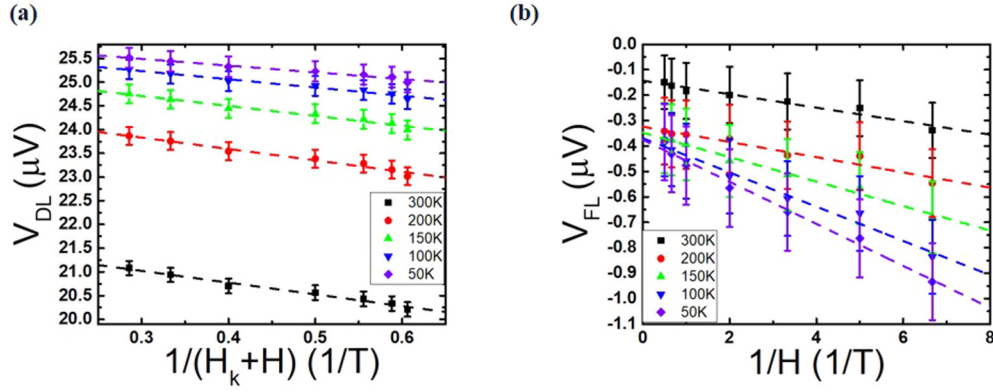
FIG. 3. (a) The contribution from the DL and (b) FL torques on the second-harmonic Hall voltage for the RS4 sample.

where H_{ext} is the applied external field, H_k is the perpendicular anisotropy field, and $I \, \alpha \, \nabla T$ is the field independent thermal contributions arising from the anomalous Nernst and Seebeck effects [38] (see Supplemental Material [36]). H_{Oe} is the Oersted field resulting from the current in the RS layer. H_{Oe} is calculated to be roughly 0.12 and 0.43 Oe at 300 K for the RS4 and RS10 samples, respectively. There is a phase shift of roughly 90° between the current direction and the field direction from sample mounting. R_{AHE} is the anomalous Hall resistance and can be extracted by sweeping an out of plane field to 3 T and is measured down to 50 K. The extracted 300 K R_{AHE} values are 9.5 and 7.9 Ω for the RS4 and RS10 samples, respectively. The V_{DL} and V_{FL} voltages are extracted via fitting the second-harmonic signals at various H_{ext} from 0.15 to 3 T and at various sample temperatures from 50 to 300 K, shown in Figs. 3(a) and 3(b). V_{DL} is fitted to a linear relation to separate the field independent thermal contributions from the DL SOT. The thermal term is the dominant contribution to V_{DL} in the samples ranging from 22 to 26 μV and 14 to 18 μV for the RS4 and RS10 samples, respectively. The field dependence of V_{FL} also has a nonzero intercept which does not fit the model in Eq. (2); we have added an additional constant term to the linear fitting. The origin of this constant offset is still unclear; however, similar offsets have been seen in materials with large thermal contributions to the second-harmonic signal such as Ta [38] and $W_x Te_{1-x}$ [41]. The extracted value of H_{FL} is about 5× larger than the calculated value of H_{Oe}, suggesting the FL term is dominant over the Oersted contributions. H_{DL} and H_{FL} are the effective fields generated from the spin currents originating in the RS layer, and have the form

$$H_{DL} = \frac{\hbar \, \zeta_{DL} \, J_{RuSn}}{2e \, M_S \, t_{CoFeB}} (\hat{\sigma} \times \hat{m}),$$

$$H_{FL} = \frac{\hbar \, \zeta_{FL} \, J_{RuSn}}{2e \, M_S \, t_{CoFeB}} [\hat{m} \times (\hat{\sigma} \times \hat{m})], \quad (3)$$

where $\hat{\sigma}$ and $\hat{m}$ are the directions of the spin polarization and magnetization, respectively. M_S is the saturation magnetization of the CoFeB layer and is measured via vibrating sample magnetometry down to 50 K, shown in Supplemental Fig. 7 [36]; the room temperature value of M_s is 1100 emu/cm³. t_{CoFeB} is the thickness of the CoFeB layer and J_{RuSn} is the estimated charge current flowing in the RS channel assuming

parallel resistors. ζ_{DL} and ζ_{FL} are the effective charge to spin conversion efficiencies for DL and FL torques, respectively. We depict the fitted values of ζ_{DL} and ζ_{FL} as a function of temperature in Figs. 3(a) and 3(b). Within a typical SOT material and FM bilayer the DL torque efficiency is from the vertical flow of spin current, whereas the FL torque efficiencies are created from the accumulation of spin polarized electrons along the SOT/FM interface.

Although both types of torque in Ru_2Sn_3 exhibit nearly linear dependence on temperature, they follow opposite trends; i.e., the magnitude DL torque increases with increasing temperature, whereas the magnitude of the FL torque decreases with increasing temperature. The opposite behavior of DL and FL torques suggests the torques are originating from separate effects. The resistivity of the RS and CoFeB layers were estimated assuming a parallel circuit model, assuming the resistivity of the RS4 and 10 are the same, shown in Supplemental Fig. 2(b) (Supplemental Material [36]) [42,43]. The resistivity of the RS layer linearly increases with a decrease in temperature, without the characteristic peak in resistivity expected from the phase transformation expected at 160 K, indicating there was no crystalline transition into the TI phase. The temperature vs resistivity observed suggests the films remained amorphous; however we still see large spin torques generated by the RS thin film, indicating the presence of large SOC. The extracted ζ_{DL} and ζ_{FL} also do not increase sharply below 160 K, which would be expected if the system transitioned into the TI phase due to the emergence of spin polarized topological surface states.

Figures 4(c) and 4(d) show the extracted spin torque efficiencies of the RS4 and RS10 samples as a function of the RS layer resistivity. The FL torque increases in magnitude from the low-resistivity room temperature measurement to a higher value in the high-resistivity low-temperature measurement. However, the DL torques follow an opposite trend with resistivity, suggesting the torques are arising from separate effects. The temperature dependent effective torque efficiencies can be analyzed by using the following equation [44,45]:

$$-\zeta = \sigma_s^{Int} \rho + \frac{\sigma_s^{SJ} \rho_0^2 + \alpha_{ss} \rho_0}{\rho}, \quad (4)$$

where ρ, ρ_0, σ_s^{Int}, σ_s^{SJ}, and α_{ss} are longitudinal resistivity, residual resistivity (resistivity at 0 K), intrinsic spin conductivity, spin conductivity due to the side jump, and skew scattering
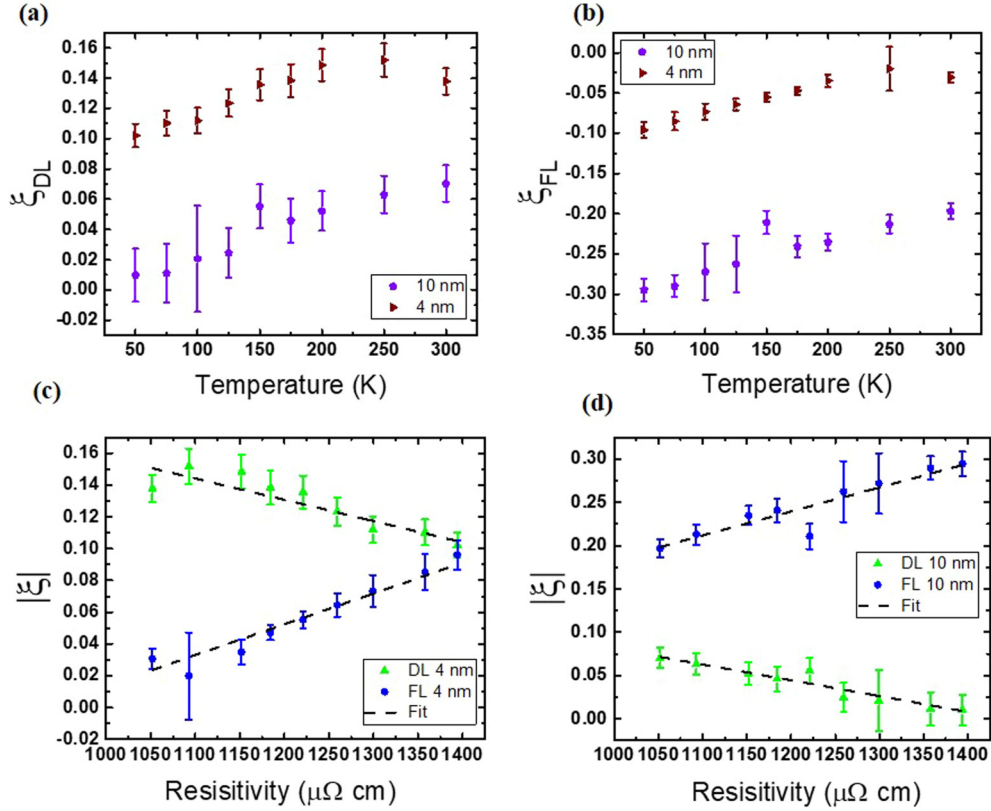
FIG. 4. (a) Temperature dependence of the SOT efficiency from the DL torque and (b) FL torque. (c), (d) Relation between magnitude $\zeta_{DL,FL}$ and the resistivity of the RS4 and RS10 samples, respectively. The dashed lines show the fit to Eq. (4).

angle, respectively. Equation (4) assumes a transparent interface between the CFB and Ru_2Sn_3 and does not consider interface effects, such as spin memory loss and spin reflections. The residual resistivity of $1450\,\mu\Omega\,cm$ is extracted from the Ru_2Sn_3 resistivity vs temperature trend in Supplemental Fig. 2(b) [36]. As shown in Figs. 3(c) and 3(d), ζ_{FL} increases monotonically with ρ indicating that the FL torque is originated from the intrinsic spin Hall effect. ζ_{FL} is larger in the RS10 compared to the RS4 sample which agrees with the intrinsic spin Hall effect mechanism. ζ_{DL} decreases with increase in ρ against the belief of intrinsic spin Hall effect. By fitting Eq (4) to the data the estimated spin Hall parameters are extracted and shown in Table I. For both RS4 and RS10 the FL torque efficiencies show larger σ_s^{Int} than their DL counterparts suggesting the FL torques are mainly originating from the intrinsic spin Hall effect. Similarly, the FL torques have smaller $\sigma_s^{SJ}\rho_0^2 + \alpha_{ss}\rho_0$ extrinsic parameters than the DL

TABLE I. Extracted intrinsic spin conductivity and extrinsic spin Hall resistivity components, side jump, and skew scattering, from fitting Eq. (4) to the DL and FL spin torques for the RS4 and RS10 samples.

	ζ	σ_s^{Int} $(\Omega\,cm)^{-1}$	$\sigma_s^{SJ}\rho_0^2 + \alpha_{ss}\rho_0$ $(\mu\Omega\,cm)$
RS4	DL	13 ± 12	-175 ± 19
RS4	FL	117 ± 10	-106 ± 15
RS10	DL	73 ± 11	-157 ± 16
RS10	FL	240 ± 19	-57 ± 27

torques, suggesting the DL torques are originating from the extrinsic spin Hall effects.

The dominant FL torque term with non-negligible DL torque seen in the RS10 sample is an atypical result. Typically, HM systems with large SOC such as Pt, W, and Ta interfaced with thick magnetic layers with in-plane magnetic anisotropy are dominated by the spin Hall effect (SHE), generating a large DL and a negligible FL term [38]. In the case of Ta, non-negligible FL torques have been observed [38,46,47]; however, the DL torque typically remains the dominant torque. In the case of HM systems interfaced with thin magnetic layers with out of plane magnetic anisotropy FL can be comparable or larger than the DL torque [4,46,48]. Additionally, inserting a Hf spacer between W and a ferromagnet has been shown to increase the FL torque to be above the DL torque [49]. However, the FL torques in the RS films have very different temperature dependence than the Ta and W/Hf devices. In those samples the FL torque has a very strong temperature dependence, decreasing almost to zero and even changing the sign of the FL torque at low temperatures while the dampinglike torque is almost temperature independent [46]. The spin swapping effect can also generate substantial FL torques and dominates in the system where the disorder is high and spin-orbit coupling is minimal [50]. The large DL torques observed in the RS films suggest a strong spin-orbit coupling, which does not fit with the spin swapping model. Large FL torques have been also observed in two-dimensional materials such as MoS_2 and WSe_2 due to a strong Rashba-Edelstein effect; however, the DL torques in the monolayer

systems are negligible since no bulk effects can contribute [51]. Bulk systems with strong interfacial Rashba torques can cause an increase in FL torque efficiency due to the increase of bulk resistivity, increasing the current flowing through the interface increasing the FL torques. The decreased current through the bulk of the RS layer would decrease the current generated via the SHE reducing the DL torque efficiency. A similar resistivity dependence of the FL torque was observed in Ta systems [46,47,52]. However, in these interfacial Rashba systems the torques are generated at the interface and have minimal thickness dependence. The FL torques observed in the RS films have significant thickness dependence indicating a bulk material dominated effect.

To study the SOT switching of a magnetic layer considering large FL torques on the order of or larger than the DL term, we performed macrospin approximation calculations; see the Supplemental Material [36], and also [53]. The inclusion of large FL components in a simulated perpendicular magnetic tunnel junction (p-MTJ) device reduces the magnetization precession and decreases the switching current by roughly 50%. For in-plane oriented magnetization we found the FL torque to have little to no impact on the switching dynamics.

IV. CONCLUSIONS

Current driven SOTs in magnetron sputtered Ru_2Sn_3/$Co_{20}Fe_{60}B_{20}$ layered structures with in-plane magnetization were investigated. We extracted the DL and FL spin torque efficiencies of the RS4 and RS10 samples utilizing the harmonic Hall technique. The calculated room temperature DL torque and FL torque for the RS4(RS10) system are 0.14 ± 0.008

(0.07 ± 0.012) and -0.03 ± 0.006 (-0.20 ± 0.009), respectively. The opposite trend of the DL and FL torques with temperature and resistivity suggests the torques arise from separate effects. The FL torques show dominant contributions from the intrinsic SHE while the DL torques show dominate contributions from the extrinsic SHE. The trend of the torque efficiencies with temperature suggests the FL torque could also arise from interfacial effects. We performed macrospin calculations of switching a perpendicular and in-plane magnetization FM layer including contributions from both the DL and FL torques. The simulations suggest that including FL torques on the order of or larger than the DL torque reduces J_c and magnetization precession for perpendicular FM layers.

[1] L. Liu, C. F. Pai, Y. Li, H. W. Tseng, D. C. Ralph, and R. A. Buhrman, Science **336**, 555 (2012).

[2] S. Manipatruni, D. E. Nikonov, and I. A. Young, Appl. Phys. Express **7**, 103001 (2014).

[3] M. Wang, Y. Zhang, X. Zhao, and W. Zhao, Micromachines **6**, 1023 (2015).

[4] J. Kim, J. Sinha, M. Hayashi, M. Yamanouchi, S. Fukami, T. Suzuki, S. Mitani, and H. Ohno, Nat. Mater. **12**, 240 (2013).

[5] Z. Zhao, M. Jamali, A. K. Smith, and J. P. Wang, Appl. Phys. Lett. **106**, 132404 (2015).

[6] Q. Hao, W. Chen, and G. Xiao, Appl. Phys. Lett. **106**, 182403 (2015).

[7] C. F. Pai, L. Liu, Y. Li, H. W. Tseng, D. C. Ralph, and R. A. Buhrman, Appl. Phys. Lett. **101**, 122404 (2012).

[8] T. J. Peterson, P. Sahu, D. Zhang, M. DC, and J. P. Wang, IEEE Trans. Magn. **55**, 1 (2019).

[9] I. M. Miron, K. Garello, G. Gaudin, P. J. Zermatten, M. V. Costache, S. Auffret, S. Bandiera, B. Rodmacq, A. Schuhl, and P. Gambardella, Nature **476**, 189 (2011).

[10] L. Liu, O. J. Lee, T. J. Gudmundsen, D. C. Ralph, and R. A. Buhrman, Phys. Rev. Lett. **109**, 096602 (2012).

[11] C.-F. Pai, Y. Ou, L. H. Vilela-Leão, D. C. Ralph, and R. A. Buhrman, Phys. Rev. B **92**, 064426 (2015).

[12] A. R. Mellnik, J. S. Lee, A. Richardella, J. L. Grab, P. J. Mintun, M. H. Fischer, A. Vaezi, A. Manchon, E. A. Kim, N. Samarth, and D. C. Ralph, Nature **511**, 449 (2014).

[13] Y. Wang, P. Deorani, K. Banerjee, N. Koirala, M. Brahlek, S. Oh, and H. Yang, Phys. Rev. Lett. **114**, 257202 (2015).

[14] M. Jamali, J. S. Lee, J. S. Jeong, F. Mahfouzi, Y. Lv, Z. Zhao, B. K. Nikolić, K. A. Mkhoyan, N. Samarth, and J. P. Wang, Nano Lett. **15**, 7126 (2015).

[15] M. DC, R. Grassi, J. Y. Chen, M. Jamali, D. Reifsnyder Hickey, D. Zhang, Z. Zhao, H. Li, P. Quarterman, Y. Lv, M. Li, A. Manchon, K. A. Mkhoyan, T. Low, and J. P. Wang, Nat. Mater. **17**, 800 (2018).

[16] M. DC, T. Liu, J. Y. Chen, T. Peterson, P. Sahu, H. Li, Z. Zhao, M. Wu, and J. P. Wang, Appl. Phys. Lett. **114**, 102401 (2019).

[17] R. Ramaswamy, T. Dutta, S. Liang, G. Yang, M. S. M. Saifullah, and H. Yang, J. Phys. D: Appl. Phys. **52**, 224001 (2019).

[18] M. DC, J.-Y. Y. Chen, T. Peterson, P. Sahu, B. Ma, N. Mousavi, R. Harjani, and J.-P. P. Wang, Nano Lett. **19**, 4836 (2019).

[19] K. Kondou, R. Yoshimi, A. Tsukazaki, Y. Fukuma, J. Matsuno, K. S. Takahashi, M. Kawasaki, Y. Tokura, and Y. Otani, Nat. Phys. **12**, 1027 (2016).

[20] Y. Fan, P. Upadhyaya, X. Kou, M. Lang, S. Takei, Z. Wang, J. Tang, L. He, L. Te Chang, M. Montazeri, G. Yu, W. Jiang, T. Nie, R. N. Schwartz, Y. Tserkovnyak, and K. L. Wang, Nat. Mater. **13**, 699 (2014).

[21] M. Z. Hasan and C. L. Kane, Rev. Mod. Phys. **82**, 3045 (2010).

[22] Y. Ando, T. Hamasaki, T. Kurokawa, K. Ichiba, F. Yang, M. Novak, S. Sasaki, K. Segawa, Y. Ando, and M. Shiraishi, Nano Lett. **14**, 6226 (2014).

[23] C. H. Li, O. M. J. Van't Erve, J. T. Robinson, Y. Liu, L. Li, and B. T. Jonker, Nat. Nanotechnol. **9**, 218 (2014).

[24] A. Manchon and S. Zhang, Phys. Rev. B **79**, 094422 (2009).

[25] T. Suzuki, S. Fukami, N. Ishiwata, M. Yamanouchi, S. Ikeda, N. Kasai, and H. Ohno, Appl. Phys. Lett. **98**, 142505 (2011).

[26] A. Manchon, H. C. Koo, J. Nitta, S. M. Frolov, and R. A. Duine, Nat. Mater. **14**, 871 (2015).

[27] H. Spring, A. R. Akhmerov, and D. Varjas, arXiv:2012.12909v2.

[28] P. Corbae, S. Ciocys, D. Varjas, S. Zeltmann, C. H. Stansbury, M. Molina-Ruiz, Z. Chen, L. W. Wang, A. M. Minor, A. G. Grushin, A. Lanzara, and F. Hellman, arXiv:1910.13412v1.

[29] P. Sahu, T. Peterson, J.-Y. Chen, X. Devaux, H. Jaffres, S. Migot, H. Dang, J.-M. George, Y. Lu, and J.-P. Wang, arXiv:1911.03323.

[30] A. S. Everhardt, M. DC, X. Huang, S. Sayed, T. A. Gosavi, Y. Tang, C.-C. Lin, S. Manipatruni, I. A. Young, S. Datta, J.-P. Wang, and R. Ramesh, Phys. Rev. Mater. **3**, 051201(R) (2019).

[31] Q. D. Gibson, D. Evtushinsky, A. N. Yaresko, V. B. Zabolotnyy, M. N. Ali, M. K. Fuccillo, J. Van Den Brink, B. Büchner, R. J. Cava, and S. V. Borisenko, Sci. Rep. **4**, 5168 (2014).

[32] D. J. Poutcharovsky, K. Yvon, and E. Parthé, J. Less-Common Met. **40**, 139 (1975).

[33] Y. Shiomi and E. Saitoh, AIP Adv. **7**, 035011 (2017).

[34] S. Zhang, Q. D. Gibson, W. Yi, J. Guo, Z. Wang, Y. Zhou, H. Wang, S. Cai, K. Yang, A. Li, Q. Wu, R. J. Cava, L. Sun, and Z. Zhao, EPL **117**, 46001 (2017).

[35] T. B. Massalski and H. Okamoto, *Binary Alloy Phase Diagrams* (ASM International, Materials Park, Ohio, 1990).

[36] See Supplemental Material at http://link.aps.org/supplemental/10.1103/PhysRevMaterials.5.045003 for additional experimental and calculation details.

[37] M. Kawaguchi, K. Shimamura, S. Fukami, F. Matsukura, H. Ohno, T. Moriyama, D. Chiba, and T. Ono, Appl. Phys. Express **6**, 113002 (2013).

[38] C. O. Avci, K. Garello, M. Gabureac, A. Ghosh, A. Fuhrer, S. F. Alvarado, and P. Gambardella, Phys. Rev. B **90**, 224427 (2014).

[39] M. Hayashi, J. Kim, M. Yamanouchi, and H. Ohno, Phys. Rev. B **89**, 144425 (2014).

[40] Y. Wen, J. Wu, P. Li, Q. Zhang, Y. Zhao, A. Manchon, J. Q. Xiao, and X. Zhang, Phys. Rev. B **95**, 104403 (2017).

[41] Y. Fan, H. Li, M. DC, T. Peterson, J. Held, P. Sahu, J. Chen, D. Zhang, A. Mkhoyan, and J. P. Wang, APL Mater. **8**, 041102 (2020).

[42] J. Liu, T. Ohkubo, S. Mitani, K. Hono, and M. Hayashi, Appl. Phys. Lett. **107**, 232408 (2015).

[43] J. Kim, P. Sheng, S. Takahashi, S. Mitani, and M. Hayashi, Phys. Rev. Lett. **116**, 097201 (2016).

[44] Y. Tian, L. Ye, and X. Jin, Phys. Rev. Lett. **103**, 087206 (2009).

[45] E. Sagasta, Y. Omori, S. Vélez, R. Llopis, C. Tollan, A. Chuvilin, L. E. Hueso, M. Gradhand, Y. C. Otani, and F. Casanova, Phys. Rev. B **98**, 060410(R) (2018).

[46] J. Kim, J. Sinha, S. Mitani, M. Hayashi, S. Takahashi, S. Maekawa, M. Yamanouchi, and H. Ohno, Phys. Rev. B **89**, 174424 (2014).

[47] X. Qiu, Z. Shi, W. Fan, S. Zhou, and H. Yang, Adv. Mater. **30**, 1705699 (2018).

[48] C. O. Avci, K. Garello, C. Nistor, S. Godey, B. Ballesteros, A. Mugarza, A. Barla, M. Valvidares, E. Pellegrin, A. Ghosh, I. M. Miron, O. Boulle, S. Auffret, G. Gaudin, and P. Gambardella, Phys. Rev. B **89**, 214419 (2014).

[49] Y. Ou, C.-F. Pai, S. Shi, D. C. Ralph, and R. A. Buhrman, Phys. Rev. B **94**, 140414(R) (2016).

[50] H. B. M. Saidaoui and A. Manchon, Phys. Rev. Lett. **117**, 036601 (2016).

[51] Q. Shao, G. Yu, Y. W. Lan, Y. Shi, M. Y. Li, C. Zheng, X. Zhu, L. J. Li, P. K. Amiri, and K. L. Wang, Nano Lett. **16**, 7514 (2016).

[52] M. Cecot, Ł. Karwacki, W. Skowroński, J. Kanak, J. Wrona, A. Zywczak, L. Yao, S. Dijken, J. Barnaś, and T. Stobiecki, Sci. Rep. **7**, 968 (2017).

[53] D. Zhu and W. Zhao, Phys. Rev. Appl. **13**, 044078 (2020).